

Hydrodynamic interactions are key in thrust-generation of hairy flagella

S. S. Asadzadeh ^{1,*} J. H. Walther ² A. Andersen ¹ and T. Kiørboe ¹

¹*Centre for Ocean Life, National Institute of Aquatic Resources, Technical University of Denmark, DK-2800 Kgs. Lyngby, Denmark*

²*Department of Mechanical Engineering, Technical University of Denmark, DK-2800 Kgs. Lyngby, Denmark and Computational Science and Engineering Laboratory, ETH, CH 8092 Zürich, Switzerland*



(Received 20 December 2021; accepted 3 June 2022; published 5 July 2022)

The important role of unicellular flagellated micro-organisms in aquatic food webs is mediated by their flagella, which enable them to swim and generate feeding currents. The flagellum in many predatory flagellates is equipped with hairs (mastigonemes) that reverse the direction of thrust compared to the thrust due to a smooth flagellum. Conventionally, the mechanism of such reversal has been attributed to drag-based thrust of individual hairs, neglecting their hydrodynamic interactions. However, at natural densities of hairs, hydrodynamic interactions are important. In fact, using fully resolved three-dimensional computational fluid dynamics, we show here that hydrodynamic interactions are key to thrust-generation and reversal in hairy flagellates, making their hydrodynamics fundamentally different from the slender-body theory governing smooth flagella. We reveal the significant role of the curvature of the flagellum, and using model analysis we demonstrate that strongly curved flagellar waveforms are optimal for thrust-generation. Our results form a basis for understanding the diverse flagellar architectures and feeding modes of predatory flagellates.

DOI: [10.1103/PhysRevFluids.7.073101](https://doi.org/10.1103/PhysRevFluids.7.073101)

I. INTRODUCTION

Eukaryotic flagella and cilia are ubiquitous in many organisms. They accomplish tasks such as locomotion in unicellular protists and spermatozoa [1,2], and feeding, pumping, and other transport functions in unicellular and multicellular organisms [3–9]. While eukaryotic flagella are fundamentally different from prokaryotic flagella in terms of structure and movement, the mechanism of thrust-generation by such often smooth (naked) and slender organelles is similar and well-understood [10–13]. The so-called drag-based thrust mechanism hinges on anisotropy in the drag coefficients of slender objects at low Reynolds number: the drag in sideways motion is larger than the drag in lengthwise motion, giving rise to a net force component perpendicular to the direction of motion when the object moves obliquely [11]. Short segments of a smooth flagellum behave locally in the same way, producing a net thrust that propels the cell [13]. In many predatory flagellates, however, the flagellum is equipped with either a vane or thick and rigid tubular hairs, known as mastigonemes [14,15]. Little is known about the hydrodynamics of such flagella despite their great significance.

Predatory flagellates are important in aquatic food webs and the marine carbon cycle [3,17–19], and their survival relies on the feeding flow generated by their hairy flagellum [20,21]. In hairy flagellates with two-dimensional flagellar wave motion, the tubular hairs are in the beat plane and perpendicular to the flagellum [22–24] [Fig. 1(a)]. The hairs cause the thrust (force acting on the

*sesasa@aqu.dtu.dk

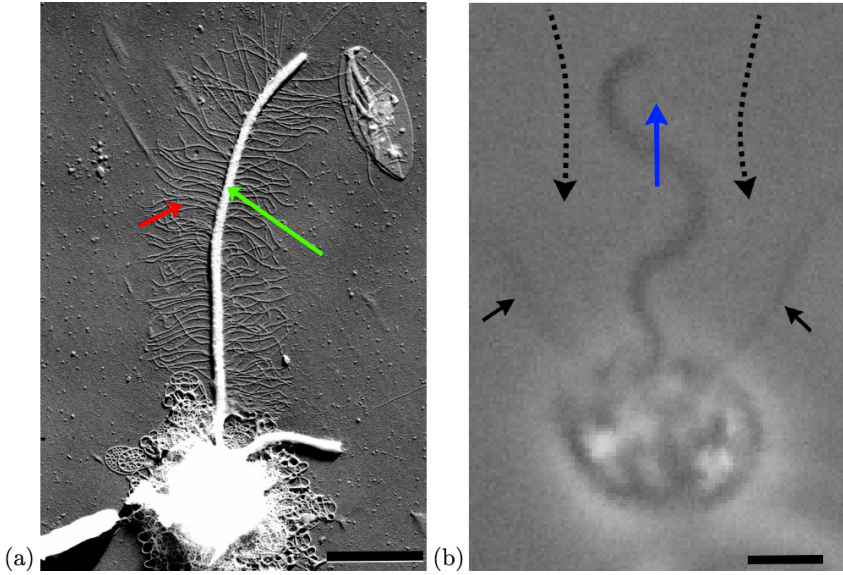


FIG. 1. Appearance and function of flagellar hairs. (a) Transmission electron micrograph of *Paraphysomonas* sp with tubular hairs (short arrow, red) on the flagellum (long arrow, green). Image courtesy of Helge A. Thomsen. (b) Light micrograph of a tethered individual of *Pteridomonas danica*. The hairy flagellum drives a feeding current (dashed arrows) towards the cell in the opposite direction of the propagating flagellar wave (blue arrow) [16], and the flow goes past the prey-intercepting tentacles extending from the cell (solid black arrows). The hairs on the flagellum are too thin to be visible in light microscopy. Image courtesy of Sei Suzuki-Tellier. Scale bars in (a) and (b): 2 μm .

hairs plus the flagellum from the water averaged over the beat cycle) to reverse compared with the thrust of a smooth flagellum and to point in the same direction as the propagating wave [Fig. 1(b)]. In a freely swimming cell, the thrust is counterbalanced by the drag force acting on the cell body, and thus the cell is pulled rather than pushed by the flagellum; in a tethered cell, the flagellum generates a feeding current towards the cell [16,22,25]. Jahn, Landman, and Fonseca qualitatively ascribed this thrust reversal to the rowing action of hairs at the crests of the wave, and they proposed that hairs provide a surface roughness resulting in thrust reversal [22]. Holwill and Sleight later implemented the aforementioned proposal and suggested that the presence of hairs on the flagellum could increase the net parallel drag coefficient of flagellum and hairs considered together and make it exceed the normal drag coefficient, hence reversing the thrust [26]. To estimate a drag coefficient for hairy flagellates, Holwill and Sleight added the coefficients of the flagellum and the individual hairs [Ref. [22], Eq. (16)], assuming that individual hairs and flagellum are hydrodynamically independent. Consequently, in such a view, the flagellum itself acts as if it is a naked flagellum, and thrust reversal relies entirely on the anisotropy in the drag coefficient of the individual hairs, similar to the analysis by Brennen [27]. However, the distance between neighboring hairs is typically much smaller than the length of the hairs, and disregarding hydrodynamic interactions appears unjustified [28]. While numerical simulations have included hydrodynamic interactions [29–31], these analyses have not elucidated the mechanism of thrust reversal in light of hydrodynamic interactions.

Here, we use three-dimensional computational fluid dynamics (CFD) to fully resolve the complex flow around hairy flagella, and we demonstrate how the hydrodynamic interactions between hairs are key in the underlying mechanism of thrust-generation in hairy flagellates. We first simulate the swimming *Pteridomonas danica* to compare the CFD predictions of the thrust and the swimming speed to observations, and to estimate the possible deflection of hairs. Thereafter, we focus on the mechanism of thrust reversal in a tethered organism, and we study the importance of hydrodynamic

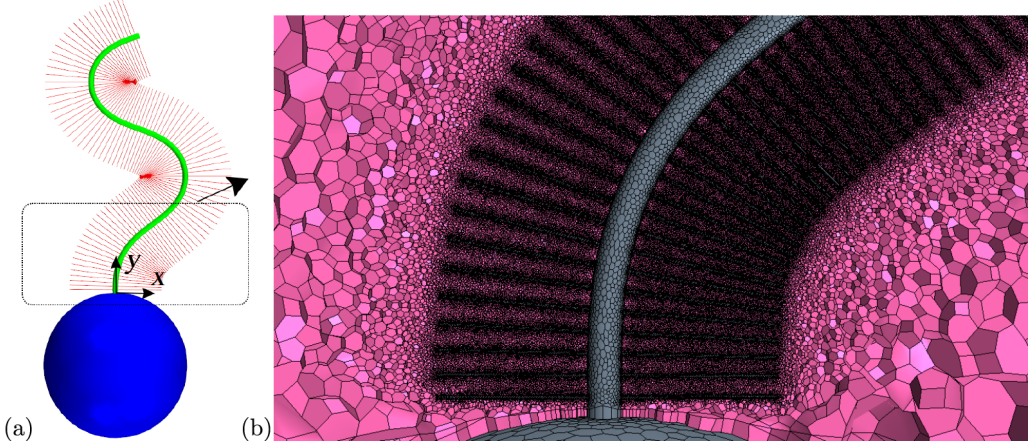


FIG. 2. Model morphology of *Pteridomonas danica* and the computational mesh. (a) The model of *P. danica* has a spherical cell (blue) of diameter $5.0 \mu\text{m}$, a flagellum (green) of length $L_f = 12.5 \mu\text{m}$ and diameter $D_f = 0.20 \mu\text{m}$, and hairs (red) each of length $l = 1.50 \mu\text{m}$ and diameter $D_h = 20 \text{ nm}$ [3,27]. (b) A snapshot of the finite volume polyhedral cells in the beat plane around the base of the flagellum.

interactions between the hairs. We propose and test a mechanism of thrust reversal based on such interactions, and we derive an analytical model of the thrust. Finally, we discuss the implications of the mechanism for the hairy flagellar architectures observed in nature.

II. METHODOLOGY

A. Model organism and morphology

The predatory flagellate *P. danica* [Fig. 1(b)] is a representative model organism [3]. The culture of *P. danica* was isolated from coastal waters (Øresund, Denmark) and maintained on a rice grain as substrate for their bacterial prey. Swimming cells were observed with an Olympus IX71 inverted microscope equipped with a UPLSAPO60XO/1.35 oil-immersion objective and video-recorded using a Phantom v210 high-speed digital camera at 1000 frames s^{-1} at a resolution of 5 pixels μm^{-1} . The beat pattern was digitized, reconstructed, and modeled following the approach by Geyer *et al.* [32]. The flagellum beats with a planar wave [Fig. 2(a)], and we use the waveform model

$$\phi(s, t) = A_\phi (1 - e^{-s/\delta}) \sin(2\pi f t - 2\pi s/\lambda_\phi), \quad (1)$$

where $\phi(s, t)$ is the angle of the tangent of the flagellum with respect to the flagellar axis, s is the arc-length from the point of attachment on the spherical cell body, t is time, $A_\phi = 2\pi/5$ is the amplitude, $\lambda_\phi = 10 \mu\text{m}$ is the wavelength, $f = 50 \text{ Hz}$ is the beat frequency, and $\delta = 2.0 \mu\text{m}$ is the amplitude modulation factor dampening the amplitude where the flagellum is attached to the cell body. These parameters are extracted from the analysis of the flagellar waveform of *P. danica*, the details of which are given in the Supplemental Material (Fig. S1) [33]. All the parameters used in the following are listed in Table I. The flagellum has approximately $13 \text{ hairs } \mu\text{m}^{-1}$ of length $l = 1.50 \mu\text{m}$ [3] in two rows along the flagellum (hence $6.5 \text{ hairs } \mu\text{m}^{-1}$ on each side). The hairs are positioned equidistantly along the flagellum and assumed to be rigid and remain perpendicular to the flagellum [27], and they are positioned slightly off the beat plane to avoid direct physical interference during the beat (see the Supplemental Material, Fig. S2). In the sheet model (a sheet instead of the dense hairs), the kinematics of the sheet follows the kinematics of the flagellum [Eq. (1)] similar to that of hairs, i.e., material points on the surface of the sheet are treated as if they were on that of a hair remaining perpendicular to the flagellum during the beat. In the study of hydrodynamic interactions among hairs, the hairs are positioned in the beat plane, and the length of the hairs is reduced from the observed length $l = 1.50$ to $0.90 \mu\text{m}$ to avoid physical interference.

TABLE I. Glossary of symbols.

Symbol	Description	Unit
A	amplitude of the displacement	μm
A_ϕ	amplitude of the angle	rad
α	shape factor of the unit	
β	tangent of angle between hairs and beat plane	
γ_{xy}	angle between hairs and beat plane	rad
C_n	drag coefficient (sideways)	
C_t	drag coefficient (lengthwise)	
d	displacement of the material points on the flagellum	μm
D_{cell}	diameter of the cell	μm
D_h	diameter of hairs	μm
D_f	diameter of the flagellum	μm
δ	amplitude modulation factor	μm
$\delta_{h,\text{max}}$	maximum deflection of hairs	μm
EI	flexural rigidity	$\text{pN } \mu\text{m}^2$
f	beat frequency	s^{-1}
$F_{h,\text{max}}$	maximum force exerted on hairs	pN
F_n	force (sideways motion)	pN
F_t	force (lengthwise motion)	pN
F_y	thrust generated by hairy flagellum	pN
$\tilde{F}_{y,\text{RFT}}$	thrust prediction of resistive force theory	pN
$\tilde{F}_{y,\text{sheet}}$	thrust generation of the sheet model	pN
$\tilde{F}_{y,\text{unit}}$	thrust generation of the basic thrust unit	pN
ϕ	angle of the tangent of the flagellum	rad
l	length of hairs	μm
L_f	length of the flagellum	μm
λ	wavelength of the displacement	μm
λ_ϕ	wavelength of the angle	μm
μ	viscosity	Pa s
N	density of hairs	μm^{-1}
Ω_{unit}	rotation rate of the hairs at the crests	rad s^{-1}
r_c	radius of the curvature of the flagellum	μm
ρ	density	kg m^{-3}
s	arc length along the flagellum	μm
σ	stress tensor	Pa
t	time	s
θ	angle between the straight edges of the basic thrust unit	rad
u	flow velocity	$\mu\text{m s}^{-1}$
U	speed of the array of hairs	$\mu\text{m s}^{-1}$
U_n	induced velocity (sideways motion)	$\mu\text{m s}^{-1}$
U_{swim}	swimming velocity	$\mu\text{m s}^{-1}$
U_t	induced velocity (lengthwise motion)	$\mu\text{m s}^{-1}$
U_{unit}	characteristic speed of the unit	$\mu\text{m s}^{-1}$

Such a reduction is expected to underestimate hydrodynamic interactions between hairs since the long-range flow field produced by individual hairs is related to their length [27].

B. Computational fluid dynamics

We use CFD to numerically solve the flow governing equations around the hairy flagellum and the cell body in water with a density of $\rho = 997 \text{ kg m}^{-3}$ and a viscosity of $\mu = 0.001 \text{ Pa s}$. We

benchmark the CFD solution against the analytical solution for a single hair, and we obtain less than 1% deviation in the drag coefficients (see the Supplemental Material, Sec. A). The computational domain is a sphere of diameter $300 \mu\text{m}$ surrounding the flagellate. The domain is discretized on a finite volume mesh and consists of polyhedral cells [Fig. 2(b)], and the discretized Navier-Stokes equations are solved using the commercial software STAR-CCM+ version 15.06.006. The average computational cell sizes around the hairs and flagellum are 5 and 50 nm, respectively, and the size of the cells increases to $1.50 \mu\text{m}$ in the far-field on the spherical outer boundary of the domain. This results in typically 3 million computational cells in total. Uniform pressure is applied on the outer boundary, and a no-slip condition on the hairs, the flagellum, and the cell body. To ensure that the results are independent of the size of the computational cells, the simulations are conducted for different computational cell sizes. For cases with 3 million and more computational cells, we find $\sim 1\%$ variation in the magnitude of the thrust (see the Supplemental Material, Fig. S3a). The motion of the flagellum is discretized in 50 time steps during a complete beat cycle when the hairs are positioned in the beat plane and 100 steps when the hairs are oriented slightly off the beat plane (see the Supplemental Material, Fig. S3b). Using the morphing technique of the STAR-CCM+ software, the computational cells are redistributed corresponding to the motion of the flagellum (Movie S1: *DynamicMesh.avi* in the Supplemental Material). Due to the low Reynolds number flow regime [11,25], the governing equations are quasisteady, and the time steps are chosen such that they ensure a smooth redistribution of the computational cells without too much distortion. Still, because of the extreme deformations of the cells due to the motion of the hairs, the finite volume mesh in the entire domain is regenerated every second time step.

Simulations are conducted for both swimming and tethered organisms. Due to the linearity of the governing equations at low Reynolds number, the swimming case is considered as a superposition of a tethered organism plus a rigid-body motion of the organism [11,34]. Accordingly, the averaged swimming velocity is computed as the time average of the instantaneous swimming velocity, which in turn is computed from a force balance between an instantaneous constraining force required to prevent the microswimmer from moving and the fluid force on the microswimmer in rigid-body motion. The forces are calculated as

$$\mathbf{F} = \iint_S (\boldsymbol{\sigma} \cdot \mathbf{n}) dS, \quad (2)$$

where $\boldsymbol{\sigma}$ is the stress tensor, and \mathbf{n} is the unit normal vector on the surface S . We focus on understanding the mechanism of thrust generation, and we therefore separate between contributions from drag due to swimming and thrust produced intrinsically by the shape-changing organism [12]. The time-averaged thrust \bar{F}_y is defined as the y -component of the force in Eq. (2) produced by the hairs plus the central flagellum in a tethered organism [Fig. 2(a)].

III. RESULTS AND DISCUSSION

A. Overall hydrodynamics of *Pteridomonas danica*

The time-averaged velocity field of *P. danica* shows that the hairy flagellum indeed produces a reversed flow towards the cell [Fig. 3(a)]. We calculate the time-averaged thrust, $\bar{F}_y = 6.8 \text{ pN}$, consistent with estimates based on the observed flow in tethered individuals [21]. Furthermore, the flow field shows that there is a relatively weak upward flow in the middle of the region swept by the hairy flagellum, and a stronger downward flow on the sides. This flow structure is consistent with the experimental observation of the flow field around a morphologically similar hairy flagellate with planar waveform [22]. Lastly, the flagellum pulls the cell with the average speed $64 \mu\text{m s}^{-1}$ [Fig. 3(b)], in agreement with the observation of the freely swimming individual.

Our simulations assume the hairs to be stiff. To test this assumption, we consider the force perpendicular to the long axis of individual hairs that may deflect them. At any instant in time, the maximum force is exerted on the hairs at the outer side of the crest of the passing wave, and it amounts to $F_{h,\text{max}} = 0.40 \text{ pN}$. Assuming that this force is applied at the tip of the hairs (an upper

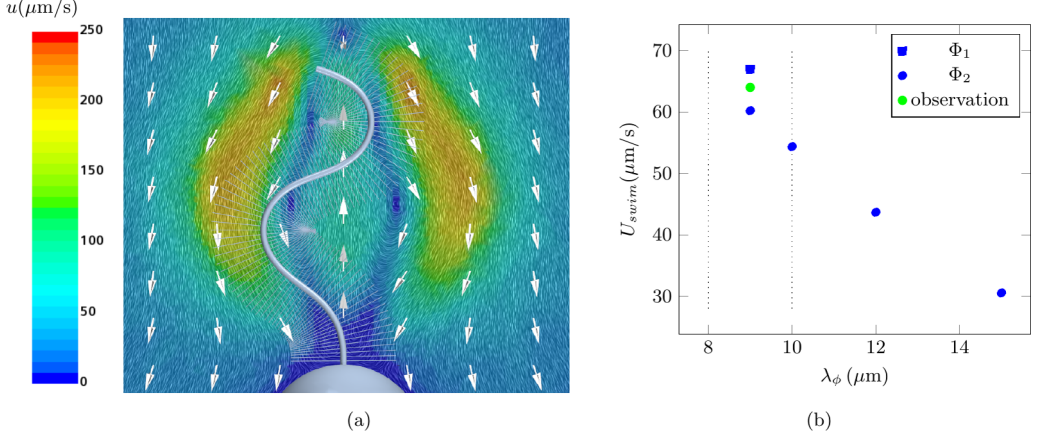


FIG. 3. Overall hydrodynamics of *Pteridomonas danica*. (a) CFD results of averaged flow field over the beat cycle at $l = 1.50 \mu\text{m}$. (b) Swimming speed at different values of λ_ϕ : in the observed range of λ_ϕ (dotted lines), there is a good agreement between CFD prediction and observation of the swimming speed. For the case with amplitude modulation factor $\delta = 1.0 \mu\text{m}$ (Φ_1), the averaged generated thrust by the flagellum $\bar{F}_y = 6.8 \text{ pN}$, consistent with indirect estimates based on observed flow fields [21], $\sim 7 \text{ pN}$. $\Phi_1 = \text{Eq. (1)}$ with $\delta = 1.0 \mu\text{m}$, and $\Phi_2 = \text{Eq. (1)}$ with $\delta = 2.0 \mu\text{m}$.

estimate) and that the hairs are clamped to the flagellum, the maximum elastic deflection at the tip of the hairs is

$$\delta_{h,\text{max}} = \frac{F_{h,\text{max}} l^3}{3EI}, \quad (3)$$

where EI is the flexural rigidity [35]. Due to a lack of data on the flexural rigidity of the tubular hairs, we use the estimated mean value of microtubules [36,37] (which have a similar diameter to that of the hairs), $EI = 22 \text{ pN } \mu\text{m}^2$, resulting in $\delta_{h,\text{max}} = 0.02 \mu\text{m}$, negligible compared to the length of the hairs ($l = 1.50 \mu\text{m}$). Accordingly, Holwill experimentally observed that the region of maximum fluid velocity is one hair length away from the central flagellum [23], which suggests that hairs are indeed relatively rigid and remain perpendicular to the flagellum.

B. Hydrodynamic interactions among hairs

To explore the hydrodynamic interactions among hairs, we simulate the flow for different densities of hairs, N , i.e., the number of hairs per unit length of the flagellum [Figs. 4(a) and 4(b)]. The presence of hairs results in thrust-reversal as compared to the smooth flagellum ($N = 0$) when $N > 1 \mu\text{m}^{-1}$ [Fig. 4(c)]. The magnitude of the thrust increases with the density of hairs, and it saturates when $N > 6 \mu\text{m}^{-1}$. This phenomenon indicates the predominance of hydrodynamic interactions among hairs in our model organism *P. danica* as well as other hairy flagellates that all have similar or higher densities [26,27]. At low densities, the flow induced by neighboring hairs on individual hairs is insignificant [Fig. 4(a)], and the thrust corresponds to the local velocity of individual hairs and thus increases when adding more hairs as long as they are hydrodynamically independent of each other. Thus, the mechanism for thrust reversal proposed by Holwill and Sleight may apply at low densities where hydrodynamic interactions are negligible [26]. However, at higher densities [Fig. 4(b)], the induced flow by neighboring hairs dominates over the local velocity of individual hairs, i.e., hydrodynamic interactions are predominant. Consequently, a further increase of the density will not generate more thrust, and several hairs, together, effectively function as a flexible, plane sheet [Fig. 4(c)]. While it is now clear that hydrodynamic interactions affect the

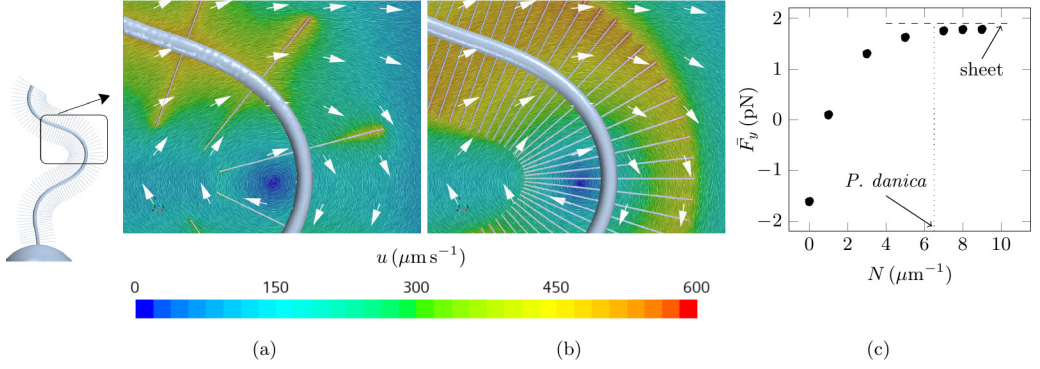


FIG. 4. Effect of the density of hairs on flow and thrust. The kinematic parameters in Eq. (1) are chosen based on the beat analysis of *Pteridomonas danica*, i.e., $f = 50$ Hz, $\lambda_\phi = 10 \mu\text{m}$, $A_\phi = 2\pi/5$, $\delta = 2.0 \mu\text{m}$, and $L_f = 12.5 \mu\text{m}$. The hairs are positioned in the beat plane, and the length of the hairs is reduced from the observed length $l = 1.50$ to $0.90 \mu\text{m}$ to avoid physical interference during the beat. Snapshots of the velocity field at (a) low density of hairs ($N = 1 \mu\text{m}^{-1}$), and (b) high (observed) density of hairs ($N = 7 \mu\text{m}^{-1}$). (c) Time-averaged thrust as a function of density of hairs (data points), and for a flexible, plane sheet ($N = \infty$) with the same thickness as that of the diameter of the hairs, and with the same beat kinematics. At high densities, as for *P. danica*, the induced flow by neighboring hairs on an individual hair becomes completely dominant over the local velocity of hairs, and hydrodynamic interactions dominate.

thrust of individual hairs, the question is whether it can significantly alter the underlying mechanism of the thrust generation.

C. Hair arrays: Hydrodynamic interactions and drag anisotropy

Here, to explore the connection between hydrodynamic interactions and drag anisotropy of individual hairs, we consider a simplified and conceptual model of a hair array. The array approximately resembles several hairs along a straight segment of the flagellum neglecting the flagellum itself. We assume that hairs along the segment have the same lateral motion. We consider parallel hairs of length l , equidistantly positioned in an array of side length l . The lateral motion of hairs is decomposed to lengthwise and sideways motions with speed U [Figs. 5(a) and 5(b)]. As expected, at low densities ($N \sim 1 \mu\text{m}^{-1}$), the magnitudes of the normal and the parallel drag on the array both increase when increasing the density of hairs, but eventually both saturate and become increasingly similar ($N > 6 \mu\text{m}^{-1}$) approaching the asymptotic value of an equivalent square sheet. The saturation results in neutralization of the drag anisotropy of an isolated hair [Fig. 5(c)]. The simplified model shows how the underlying mechanism for the thrust reversal in hairy flagellates ($N \simeq 6 \mu\text{m}^{-1}$) cannot rely on the drag anisotropy of individual hairs.

To shed light on the hydrodynamic interactions and their effect on drag anisotropy, we analytically explore the interactions between two parallel hairs in lengthwise and sideways motions with speed U . The low Reynolds number forces on the second hair $F_t^{(2)}$ and $F_n^{(2)}$ in lengthwise and sideways motions, respectively, are proportional to the velocity of the hair relative to the local background flow $U_t^{(2-1)}$ and $U_n^{(2-1)}$ induced by the first hair [38,39]. We can therefore write

$$F_t^{(2)} = C_t \mu l (U - U_t^{(2-1)}), \quad (4)$$

$$F_n^{(2)} = C_n \mu l (U - U_n^{(2-1)}), \quad (5)$$

where C_t and C_n are the drag coefficients for a single hair in lengthwise and sideways motion, respectively (Ref. [40], Eqs. 5-11.52 and 5-11.54). As an approximation of the induced velocity past the second hair, consider the velocity in the parallel and the normal direction due to a point force

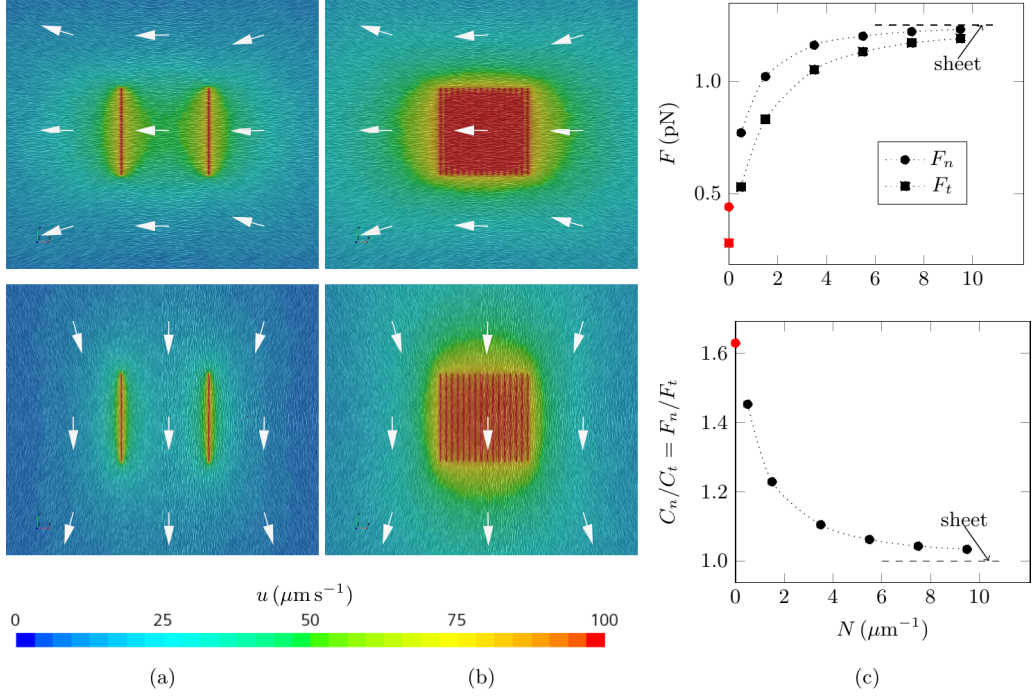


FIG. 5. Hydrodynamic interactions among parallel hairs in sideways and lengthwise motion. Both the length of the hairs and the sideways length of the arrays are $l = 2.0 \mu\text{m}$, and the diameter of the hairs is 20 nm. (a) The induced flow by one hair on the other one, i.e., the hydrodynamic interactions between two hairs ($N = 0.5 \mu\text{m}^{-1}$), is stronger when they move sideways than when they move lengthwise. (b) By adding more hairs and increasing their density, $N = 7.5 \mu\text{m}^{-1}$, the flows become similar for the two directions of motion. (c) The drag on the array in sideways, F_n , and lengthwise, F_t , motion approaches the asymptotic value of an equivalent square sheet (top), and the drag anisotropy of the system vanishes (bottom). The theoretical prediction for a single hair (red symbols) is $F_n/F_t = 1.6$, in agreement with the CFD results, and the theoretical analysis of two hairs in Eq. (8) predicts $F_n^{(2)}/F_t^{(2)} = 1.4$, in agreement with the CFD simulations for two hairs, i.e., $N = 0.5 \mu\text{m}^{-1}$.

positioned at the center of the first hair and with the same magnitude as the drag on an individual hair [11]:

$$U_t^{(2-1)} \approx \frac{F_t}{8\pi\mu l} = \frac{C_t U}{8\pi}, \quad (6)$$

$$U_n^{(2-1)} \approx \frac{F_n}{4\pi\mu l} = \frac{C_n U}{4\pi}. \quad (7)$$

Hence, the drag ratio in such a system of two hairs can be approximated:

$$\frac{F_n^{(2)}}{F_t^{(2)}} \approx \frac{C_n(1 - \frac{C_n}{4\pi})}{C_t(1 - \frac{C_t}{8\pi})} < \frac{C_n}{C_t}. \quad (8)$$

The approximation gives $F_n^{(2)}/F_t^{(2)} = 1.4$ for two hairs with similar dimensions of hairs as in Fig. 5(a), in good agreement with the CFD simulations [Fig. 5(c)]. The above analysis shows that the hydrodynamic interactions reduce the strength of the drag anisotropy because $U_n^{(2-1)} > U_t^{(2-1)}$.

D. Mechanism of thrust reversal

Here we test and explore the mechanism of thrust generation in hairy flagellates. In the previously suggested mechanism where hydrodynamic interactions are not predominant [26,27], the hairs give rise to the thrust reversal when they are along the straight parts of the flagellum during the beat. To examine the validity of such predictions, we simulate a one-quarter-wavelength-long segment of a flagellum with dense hairs and one with sparse hairs. While a long flagellum would comprise several segments, we neglect the long-range hydrodynamic interactions between segments. The segment can be thought of as the simplest thrust unit of the hairy flagellum, which accounts for the hydrodynamic interactions between neighboring hairs as well as between the flagellum and hairs. Here we choose a simple wave model for the flagellar kinematics in order to directly compare our results with known expressions based on resistive force theory [26,27]:

$$d(y, t) = A \sin(2\pi f t - 2\pi y/\lambda), \quad (9)$$

where d is the displacement of the material points on the flagellum in the lateral x -direction, y is the centerline axis, A is the amplitude, and λ is the wavelength. In the sparse system, the thrust correlates with the motion of individual hairs, and accordingly, only hairs at the straight part with a dominant transversal motion generate thrust, whereas the hairs at the crest with a dominant rotational motion do not contribute [Figs. 6(a) and 6(b)]. Conversely in the dense system, the role switches and most of the thrust is generated at the crest [Figs. 6(c) and 6(d)]. Thus, hydrodynamic interactions significantly reduce the strength of the anisotropy in drag of individual hairs when hairs are closer to each other (similar to the conceptual model of hair arrays, Sec. III C). The resulting $T/4$ phase shift ($T = 1/f$ being the period of the flagellar wave) of the generated thrust due to the hairs from the sparse to the dense system is a signature that the location of thrust-generation is shifted from the straight parts to the crests of the passing wave [Fig. 6(e)]. [Note that Eq. (9) does not automatically preserve the arc-length of the segment, and with preserved arc-length the thrust at the straight part is further reduced to negative values, while it is augmented at the crests; see the Supplemental Material, Fig. S4.] It should be noted that in both systems, the force produced by the (central) flagellum counteracts the force produced by the hairs [Fig. 6(e)].

For a quantitative comparison with resistive force theory (RFT), we consider the time-averaged drag-based thrust generated by a single hair, which in RFT is [21,26,27]

$$\bar{F}_{y, \text{RFT}} = 2(C_n - C_t)\mu l \left(1 - \frac{1}{\sqrt{1 + (2\pi A/\lambda)^2}}\right) \lambda f. \quad (10)$$

The thrust expression is proportional to the difference between C_n and C_t , emphasizing the significance of drag anisotropy in drag-based thrust [12]. Resistive force theory overestimates the thrust slightly in the sparse system but significantly in the dense system, and in both cases it is nearly insensitive to the wavelength [Fig. 6(f)]. However, according to the CFD predictions, the thrust has a weak dependence on the wavelength for the sparse system, but in contrast in the dense system, the thrust increases significantly with decreasing wavelength, indicating the change of the mechanism and highlighting the potential role of the curvature of the flagellum in thrust-generation.

E. Analytical model of the thrust

The dominance of hydrodynamic interactions in hairy flagellates with dense hairs rules out a mechanism based on anisotropy in drag of individual hairs at the straight part of the flagellum, because now several neighboring hairs, together, hydrodynamically function similar to a plane sheet [Figs. 7(a) and 7(b)]. However, the hydrodynamic interactions facilitate another mechanism of thrust-generation, thanks to the curvature of the flagellum. The curvature modifies the distance between the hairs, bringing about a difference in the area occupied by several hairs at either side of the flagellar crest [Fig. 7(c)]. This difference in the areas moving in the opposite direction due to the

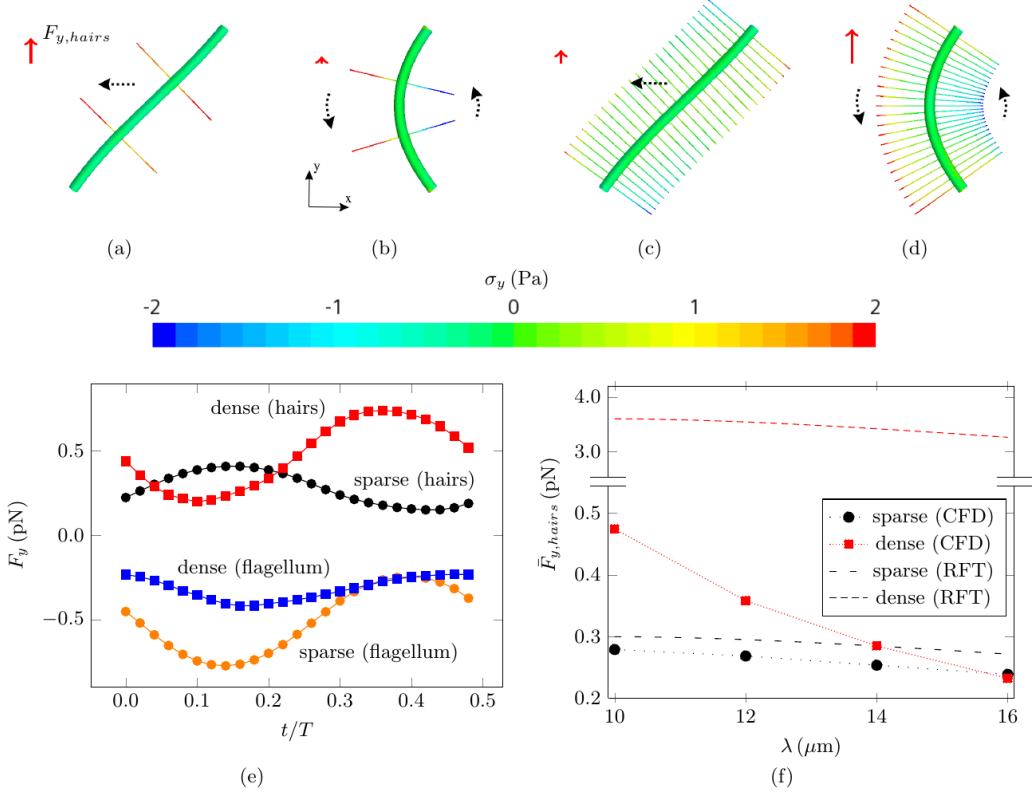


FIG. 6. Location of thrust-generation on flagella with sparse and dense hairs. We apply the kinematics in Eq. (9), and in (a)–(e) we use $f = 27.5$ Hz, $\lambda = 12 \mu\text{m}$, $A = 2.0 \mu\text{m}$, $0 < y < 3 \mu\text{m}$, and $l = 0.90 \mu\text{m}$. The dashed arrows show the overall motion of the hairs, and the red arrows show the thrust due to the hairs, $\bar{F}_{y,hairs}$. (a), (b) In the sparse system with $N = 0.8 \mu\text{m}^{-1}$, $\bar{F}_{y,hairs}$ is produced at the straight segment of the flagellum. (c), (d) In contrast, in the dense system with $N = 6.8 \mu\text{m}^{-1}$, $\bar{F}_{y,hairs}$ is produced at the curved part. (e) The thrust of the hairs and (central) flagellum in the sparse and the dense system during half of the beat period. Snapshots in (a), (c) and (b), (d) correspond to $t/T = 0.14$ and 0.38 , respectively. (f) The averaged thrust (over the beat cycle) due to the hairs as a function of the wavelength and with all other parameters as in (a)–(e). The thrust in the sparse system depends only weakly on the wavelength and is described well by the resistive force theory (RFT) model in Eq. (10), whereas the thrust in the dense system decreases strongly with increasing wavelength (decreasing curvature), and it is significantly overestimated by resistive force theory.

action of the flagellum results in a net thrust. Therefore, the basic thrust unit lies at the curvature of the flagellum rather than in the straight part.

To explore the dependence of the thrust on the flagellar architecture and waveform, consider the waveform in Eq. (1). For simplicity, we assume that the amplitude modulation factor, δ , the diameter of the flagellum, the diameter of the hairs, and the presence of the cell body only affect the thrust weakly, and therefore the remaining parameters are μ , f , λ_ϕ , A_ϕ , L_f , and l . Furthermore, we restrict attention to flagella with dense hairs ($N > 6 \mu\text{m}^{-1}$) that effectively function as a sheet [Figs. 7(a) and 7(b)]. From the parameters μ , f , λ_ϕ , A_ϕ , L_f , and l , we have three dimensionless parameters l/λ_ϕ , A_ϕ , and L_f/λ_ϕ , and in our minimal model we can express the thrust:

$$\bar{F}_y = \mu f \lambda_\phi^2 \Phi(l/\lambda_\phi, A_\phi, L_f/\lambda_\phi), \quad (11)$$

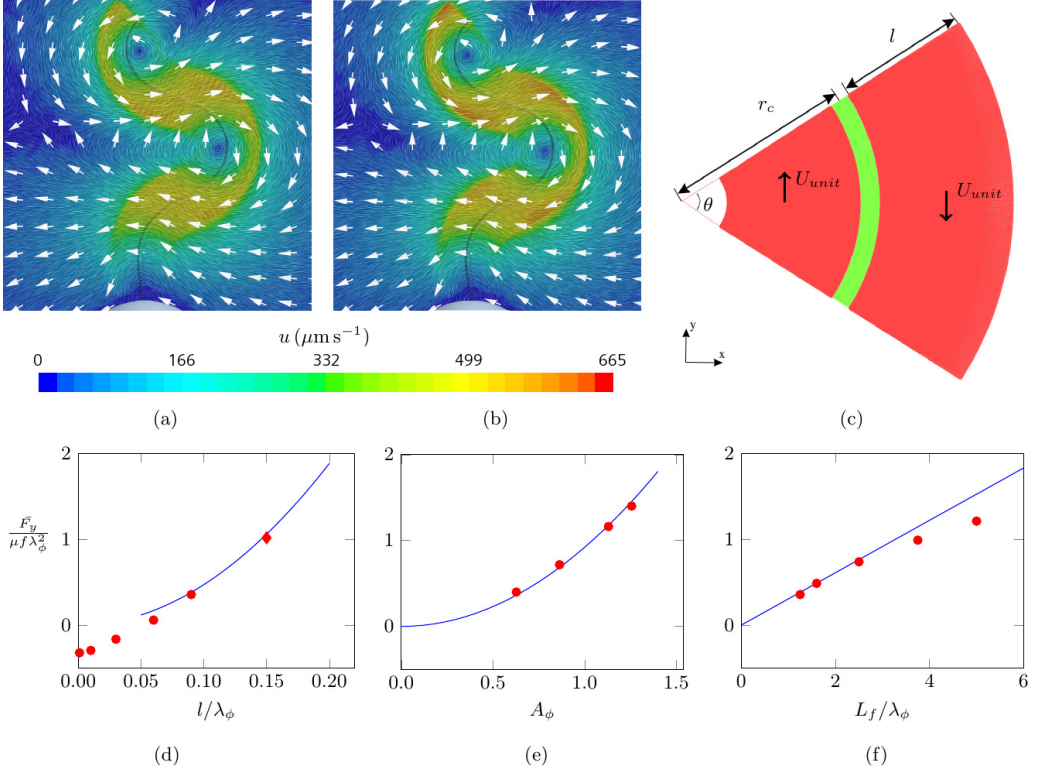


FIG. 7. Parameter exploration and analytical thrust model. (a) Snapshot of the velocity field for a hairy flagellum with the kinematics in Eq. (1) and the parameters $f = 50$ Hz, $\lambda_\phi = 10$ μm , $A_\phi = 2\pi/5$, $\delta = 2.0$ μm , $L_f = 12.5$ μm , $l = 0.90$ μm , and $N = 7$ μm^{-1} . (b) Snapshot of the velocity field produced by an equivalent plane sheet. (c) Basic thrust unit assuming that the dense system of hairs functions as a sheet (red) on either side of the flagellum (green). (d)–(f) Dimensionless thrust as a function of the dimensionless parameters l/λ_ϕ , A_ϕ , and L_f/λ_ϕ . (d) Parameters: $\lambda_\phi = 10$ μm , $A_\phi = 2\pi/5$, and $L_f = 12.5$ μm . (e) Parameters: $\lambda_\phi = 9.0$ μm , $L_f = 12.5$ μm , and $l = 1.50$ μm . (f) Parameters: $\lambda_\phi = 10$ μm , $A_\phi = 2\pi/5$, and $l = 0.90$ μm . The diamond refers to the case with $l = 1.50$ μm , where hairs are slightly off the beat plane to avoid physical interference [Fig. 3(a)]. In all CFD simulations, we used $f = 50.0$ Hz and $N = 8$ μm^{-1} . CFD results (red points) and analytical model in Eq. (14) with $\alpha = 3.80$ (blue curves).

where Φ is a dimensionless function. From dimensional analysis it is clear that \bar{F}_y is proportional to μ and f , and our CFD simulations in the three-dimensional parameter space spanned by l/λ_ϕ , A_ϕ , and L_f/λ_ϕ suggest that \bar{F}_y depends quadratically on l and A_ϕ and linearly on L_f ; cf., Figs. 7(d)–7(f).

To rationalize our findings and develop a mechanistic model, we assume that the basic thrust-generating unit is a segment of the hairy flagellum spanning one-quarter of the wavelength, similar to segments in Figs. 6(c) and 6(d). It is assumed that the thrusts are produced once the unit is centered at the crest [Fig. 7(c)]. This unit consists of two parts on either side of the flagellum where the hairs come close and fan out, respectively. The part where the hairs come close moves upwards and creates a negative thrust, whereas the part where the hairs fan out moves downwards and creates a positive thrust. The net thrust of the basic thrust unit, $\bar{F}_{y, \text{unit}}$, is the difference between the two contributions, and we make the low Reynolds number estimate:

$$\bar{F}_{y, \text{unit}} \propto \mu[\theta(r_c + l/2) - \theta(r_c - l/2)]U_{\text{unit}} = \mu\theta l U_{\text{unit}}, \quad (12)$$

where U_{unit} is the characteristic speed of the two parts, $\theta(r_c - l/2)$ is the characteristic length of the part where the hairs come close, and $\theta(r_c + l/2)$ is the characteristic length of the part where the hairs fan out [Fig. 7(c)]. (See the Supplemental Material, Fig. S5 for the argument on why force is proportional to these lengths.) Note that $\theta = \sqrt{2}A_\phi$ if the unit spans one-quarter of the wavelength. To estimate U_{unit} , we use the magnitude of the rotation rate of the hairs at the crests, $\Omega_{\text{unit}} = 2\pi f A_\phi$, since $\partial\phi/\partial t = 2\pi f A_\phi \cos(2\pi ft - 2\pi s/\lambda_\phi)$. Therefore, we obtain that $U_{\text{unit}} = \Omega_{\text{unit}} l/2 = \pi f A_\phi l$. By combining the expressions, we find the estimate

$$\bar{F}_{y, \text{unit}} = \pi \alpha \mu f A_\phi^2 l^2. \quad (13)$$

There are $2L_f/\lambda_\phi$ thrust-generating units along the full length of the flagellum, and the total thrust generated by the hairy flagellum becomes

$$\bar{F}_{y, \text{sheet}} = \frac{2L_f}{\lambda_\phi} \bar{F}_{y, \text{unit}} = 2\pi \alpha \mu f l^2 \frac{L_f}{\lambda_\phi} A_\phi^2, \quad (14)$$

where α is a shape factor. The model captures the parameter dependencies of \bar{F}_y that we find in our CFD simulations [Figs. 7(d)–7(f)], and it rationalizes how \bar{F}_y depends on l , L_f/λ_ϕ , and A_ϕ . The quadratic dependency on l could be expected as the contributions of the hairs on the two sides of the flagellum cancel to linear order, and the nearly linear dependency on L_f/λ_ϕ is a sign of weak hydrodynamic interactions between the segments, as assumed above. Moreover, the quadratic dependency on A_ϕ could be expected since a change of the sign of A_ϕ does not change the magnitude of the thrust generation.

It is worth highlighting the key role of the flagellar curvature ($=2\pi A_\phi/\lambda_\phi$ at the crest of the passing wave). The proposed mechanism results in a stronger dependence of the thrust on the wavelength in a densely haired compared to a naked flagellum, as also observed in Fig. 6(f). A flagellum with short hairs functions like a slender body with negative drag-based thrust, but as hairs become longer, the hydrodynamic interaction-based thrust becomes dominant, resulting in the reversal of the thrust [Fig. 7(d)]. Note that the negative drag-based offset (due to the central flagellum) is also affected by the dominance of the new mechanism among long hairs, becoming weaker in the dense system as compared to the sparse system [Fig. 6(e)].

IV. PERSPECTIVE

The optimal design of a flagellum with respect to thrust production is suggested by Eq. (14): The flagellum should be long, curvy (with short wavelength), and equipped with long hairs. Indeed, hairy flagella have shorter wavelength than naked flagella [16]. However, for a planar beat, as in our model organism, hairs longer than the radius of curvature at the crests would physically interfere with each other. One solution is to orient hairs slightly off the beat plane, but this implies marginally less thrust than if hairs were in the beat plane (see the Supplemental Material, Fig. S2). This solution is used by flagellates where hairs are oriented at a small angle relative to the beat plane defined by the central pair of axonemal microtubules [41,42]. A second solution, as found in many species, may be bundling of hairs [41] (i.e., three to four hairs protruding from the same attachment point on the flagellum), where interference is avoided if hairs become aligned rather than intertwined. Thirdly, the beat of the flagellum itself may not be perfectly planar [41], and many hairy flagellates in fact have complex three-dimensional beat patterns [3,43], providing room for longer hairs without interference. Yet another way to increase hydrodynamic interaction based thrust is through terminal branching of the hairs, as found in many species [41], which may significantly increase the thrust. This is potentially possible because terminal filaments occupy a larger area at one side of the crests (of the wave) than the other side, taking further advantage of the mechanism. Finally, the fibrous hairs between the tubular hairs in some species make the hairs further resemble a sheet and increase the functional rigidity of the hairs [41]. The diverse flagella designs observed in nature and discussed above can thus all be understood in the context of the mechanism for thrust production suggested

here, and they may provide novel ideas for the design of artificial swimmers and flow generation in microfluidic devices.

The presence of hairs on the flagellum is key to foraging in flagellates. Not only does the reversal of the flow increase the capture efficiency of prey arriving in the feeding current [21], but the hairs also increase the thrust generation significantly as compared to a smooth flagellum with the same beat kinematics or the same power expenditure. For a comparison of the efficiency of the thrust generation by naked versus hairy flagella, consider the following example: A hairy flagellum with $l = 1.5 \mu\text{m}$ gives a time-averaged thrust of $\bar{F}_{y,1.5} = 5.1 \text{ pN}$ with a time-averaged power expenditure of $\bar{P}_{1.5} = 24 \text{ fW}$ (Sec. III A), and a naked flagellum with the same kinematics gives $\bar{F}_{y,0} = 1.6 \text{ pN}$ and $\bar{P}_0 = 5.5 \text{ fW}$. Change in the thrust, and hence load on the flagellum, may result in a change in the frequency of the flagellar beat as observed for flagella beating at an increased viscosity [44]. Adjusting the frequency (multiplying by a factor of $5.1/1.6 = 3.2$), such that the naked flagellum produces the same thrust as the hairy flagellum, results in a modified power of $\bar{P}_{0,m} = 54 \text{ fW}$, approximately 2.2 times higher than that of the hairy flagellum. While the optimum waveform for a naked flagellum might differ marginally from that of the hairy one, this example shows that, in terms of the produced thrust, the addition of hairs is significantly more efficient than simply increasing the frequency in a naked flagellum.

The hydrodynamics of flagella is most often studied in the context of propulsion [7,11,12]. However, for predatory flagellates, the main consumers of bacteria in the ocean, efficient foraging is likely a much more important component of their fitness than propulsion per se. It should be noted that the reversal will also impact the predating risk since the stirring generated by the feeding current exposes the cells to their flow-sensing predators [45,46]. The suggested mechanism for thrust production and the associated tradeoffs motivate future and more comprehensive studies of the very diverse flagella designs found among predatory flagellates in nature. At low Reynolds number, viscosity impedes predator-prey contact, but the hairy flagellum yields the necessary force (a direct measure of the feeding current) and feeding current structure to secure the success and key role of flagellates in the microbial food webs.

ACKNOWLEDGMENTS

We are thankful for help from Tom Fenchel, Poul Scheel Larsen, Lasse Tor Nielsen, Sei Suzuki-Tellier, and Helge A. Thomsen. We received funding from The Independent Research Fund Denmark (7014-00033B) and the Carlsberg Foundation (CF17-0495). The Centre for Ocean Life is supported by the Villum Foundation.

-
- [1] G. I. Taylor, The action of waving cylindrical tails in propelling microscopic organisms, *Proc. R. Soc. London A* **211**, 225 (1952).
 - [2] H. C. Berg, *Random Walks in Biology*, expanded ed. (Princeton University Press, Princeton, NJ, 1993).
 - [3] T. Fenchel, Ecology of heterotrophic microflagellates. I. some important forms and their functional morphology, *Mar. Ecol. Prog. Ser.* **8**, 211 (1982).
 - [4] M. B. Short, C. A. Solari, S. Ganguly, T. R. Powers, J. O. Kessler, and R. E. Goldstein, Flows driven by flagella of multicellular organisms enhance long-range molecular transport, *Proc. Natl. Acad. Sci. USA* **103**, 8315 (2006).
 - [5] S. P. Leys and D. I. Eerkes-Medrano, Feeding in a calcareous sponge: Particle uptake by pseudopodia, *Biol. Bull.* **211**, 157 (2006).
 - [6] S. P. Leys, G. Yahel, A. Reidenbach, V. Tunnicliffe, U. Shavit, and H. Reiswig, The sponge pump: The role of current induced flow in the design of the sponge body plan, *PLoS ONE* **6**, e27787 (2011).
 - [7] J. S. Guasto, R. Rusconi, and R. Stocker, Fluid mechanics of planktonic microorganisms, *Annu. Rev. Fluid Mech.* **44**, 373 (2012).

- [8] R. E. Goldstein, Green algae as model organisms for biological fluid dynamics, *Annu. Rev. Fluid Mech.* **47**, 343 (2015).
- [9] W. Gilpin, M. S. Bull, and M. Prakash, The multiscale physics of cilia and flagella, *Nat. Rev. Phys.* **2**, 74 (2020).
- [10] J. Gray and G. J. Hancock, The propulsion of sea-urchin spermatozoa, *J. Exp. Biol.* **32**, 802 (1955).
- [11] E. Lauga and T. R. Powers, The hydrodynamics of swimming microorganisms, *Rep. Prog. Phys.* **72**, 096601 (2009).
- [12] E. Lauga, *The Fluid Dynamics of Cell Motility* (Cambridge University Press, Cambridge, 2020).
- [13] M. F. Velho Rodrigues, M. Lisicki, and E. Lauga, The bank of swimming organisms at the micron scale (BOSO-micro), *PLoS ONE* **16**, e0252291 (2021).
- [14] J. L. Mah, K. K. Christensen-Dalsgaard, and S. P. Leys, Choanoflagellate and choanocyte collar-flagellar systems and the assumption of homology, *Evol. Dev.* **16**, 25 (2014).
- [15] Ø. Moestrup, Flagellar structure in algae: A review, with new observations particularly on the chrysophyceae, phaeophyceae (fucophyceae), euglenophyceae, and reckertia, *Phycologia* **21**, 427 (1982).
- [16] M. A. Sleight, Flagellar movement of the sessile flagellates *Actinomonas*, *Codonosiga*, *Monas*, and *Poteriodendron*, *J. Cell Sci.* **s3-105**, 405 (1964).
- [17] F. Azam, T. Fenchel, J. G. Field, J. S. Gray, L. A. Meyer-Reil, and F. Thingstad, The ecological role of water-column microbes in the sea, *Mar. Ecol. Prog. Ser.* **10**, 257 (1983).
- [18] A. Z. Worden, M. J. Follows, S. J. Giovannoni, S. Wilken, A. E. Zimmerman, and P. J. Keeling, Rethinking the marine carbon cycle: Factoring in the multifarious lifestyles of microbes, *Science* **347**, 1257594 (2015).
- [19] T. Weisse, R. Anderson, H. Arndt, A. Calbet, P. J. Hansen, and D. J. S. Montagnes, Functional ecology of aquatic phagotrophic protists—concepts, limitations, and perspectives, *Eur. J. Protist.* **55**, 50 (2016).
- [20] T. Kiørboe, How zooplankton feed: Mechanisms, traits and trade-offs, *Biol. Rev.* **86**, 311 (2011).
- [21] S. Suzuki-Tellier, A. Andersen, and T. Kiørboe, Mechanisms and fluid dynamics of foraging in heterotrophic nanoflagellates, *Limnol. Oceanogr.* **67**, 1287 (2022).
- [22] T. L. Jahn, M. D. Landman, and J. R. Fonseca, The mechanism of locomotion of flagellates. II. Function of the mastigonemes of *Ochromonas*, *J. Protozool.* **11**, 291 (1964).
- [23] M. E. J. Holwill and P. D. Peters, Dynamics of the hispid flagellum of *Ochromonas danica*: The role of mastigonemes, *J. Cell Biol.* **62**, 322 (1974).
- [24] M. A. Sleight, Flagellar beat patterns and their possible evolution, *Biosystems* **14**, 423 (1981).
- [25] M. A. Sleight, Mechanisms of flagellar propulsion, *Protoplasma* **164**, 45 (1991).
- [26] M. E. J. Holwill and M. A. Sleight, Propulsion by hispid flagella, *J. Exp. Biol.* **47**, 267 (1967).
- [27] C. Brennen, Locomotion of flagellates with mastigonemes, *J. Mechanochem. Cell Motil.* **3**, 207 (1976).
- [28] B. Rodenborn, C.-H. Chen, H. L. Swinney, B. Liu, and H. P. Zhang, Propulsion of microorganisms by a helical flagellum, *Proc. Natl. Acad. Sci. USA* **110**, E338 (2013).
- [29] L. J. Fauci, A computational model of the fluid dynamics of undulatory and flagellar swimming, *Am. Zool.* **36**, 599 (1996).
- [30] S. Kobayashi, R. Watanabe, T. Oiwa, and H. Morikawa, Computational study of micropropulsion mechanism in water modeled on flagellum with projecting mastigonemes, *J. Biomech. Sci. Engng.* **4**, 11 (2009).
- [31] S. Namdeo, S. N. Khaderi, M. J. den Toonder, and P. R. Onck, Swimming direction reversal of flagella through ciliary motion of mastigonemes, *Biomicrofluidics* **5**, 034108 (2011).
- [32] V. F. Geyer, P. Sartori, B. M. Friedrich, F. Jülicher, and J. Howard, Independent control of the static and dynamic components of the *Chlamydomonas* flagellar beat, *Curr. Biol.* **26**, 1098 (2016).
- [33] See Supplemental Material at <http://link.aps.org/supplemental/10.1103/PhysRevFluids.7.073101> for the benchmark study of a single hair, details of the model of the beat pattern of the model organism, a model of the nonplanar hairs, a computational mesh convergence study, thrust generated with a preserved arc-length of the case in Fig. 6, and an illustration of the proposed mechanism.
- [34] S. S. Asadzadeh, L. T. Nielsen, J. Dölger, A. Andersen, T. Kiørboe, P. S. Larsen, and J. H. Walther, Hydrodynamic functionality of the lorica in choanoflagellates, *J. R. Soc. Interface.* **16**, 20180478 (2019).
- [35] J. M. Gere and B. J. Goodno, *Mechanics of Materials* (Cengage Learning, Stamford, CT, 2012).

- [36] G. B. Bouck, Extracellular microtubules: The origin, structure, and attachment of flagellar hairs in *Fucus* and *Ascophyllum* antherozoids, *J. Cell Biol.* **40**, 446 (1969).
- [37] F. Gittes, B. Mickey, J. Nettleton, and J. Howard, Flexural rigidity of microtubules and actin filaments measured from thermal fluctuations in shape, *J. Cell Biol.* **120**, 923 (1993).
- [38] Y. Man, L. Koens, and E. Lauga, Hydrodynamic interactions between nearby slender filaments, *Europhys. Lett.* **116**, 24002 (2016).
- [39] R. E. Goldstein, E. Lauga, A. I. Pesci, and M. R. E. Proctor, Elastohydrodynamic synchronization of adjacent beating flagella, *Phys. Rev. Fluids* **1**, 073201 (2016).
- [40] J. Happel and H. Brenner, *Low Reynolds Number Hydrodynamics*, 2nd ed. (Kluwer Academic, Dordrecht, 1983).
- [41] G. B. Bouck, The structure, origin, isolation, and composition of the tubular mastigonemes of the *Ochromonas* flagellum, *J. Cell Biol.* **50**, 362 (1971).
- [42] P. Sartori, V. F. Geyer, A. Scholich, F. Jülicher, and J. Howard, Dynamic curvature regulation accounts for the symmetric and asymmetric beats of *Chlamydomonas* flagella, *eLIFE* **5**, e13258 (2016).
- [43] K. K. Christensen-Dalsgaard and T. Fenchel, Complex flagellar motions and swimming patterns of the flagellates *Paraphysomonas vestita* and *Pteridomonas danica*, *Protist* **155**, 79 (2004).
- [44] G. S. Klindt, C. Ruloff, C. Wagner, and B. M. Friedrich, Load Response of the Flagellar Beat, *Phys. Rev. Lett.* **117**, 258101 (2016).
- [45] T. Kiørboe and A. G. Hirst, Shifts in mass scaling of respiration, feeding, and growth rates across life-form transitions in marine pelagic organisms, *Am. Nat.* **183**, E118 (2014).
- [46] L. T. Nielsen and T. Kiørboe, Foraging trade-offs, flagellar arrangements, and flow architecture of planktonic protists, *Proc. Natl. Acad. Sci. USA* **118**, e2009930118 (2021).